Evidence for tropospheric wind shear excitation of high phase-speed gravity waves reaching the mesosphere using ray tracing technique

M. Pramitha[1], M. Venkat Ratnam[1]*, Alok Taori[1], B. V. Krishna Murthy[2], D. Pallamraju[3], and S. Vijaya Bhaskara Rao[4]

[1]National Atmospheric Research Laboratory (NARL), Gadanki, India.

[2]B1, CEBROS, Chennai, India.

[3]Physical Research Laboratory (PRL), Ahmadabad, India

[4]Department of Physics, Sri Venkateswara University, Tirupati, India

* vratnam@narl.gov.in , Phone: +91-8585-272123, Fax: +91-8585-272018

Abstract

Sources and propagation characteristics of high-frequency gravity waves observed in the mesosphere using airglow emissions from Gadanki (13.5^{o}N, 79.2^{o}E) and Hyderabad (17.5^{o}N, 78.5^{o}E) are investigated using reverse ray tracing. Wave amplitudes are also traced back including both radiative and diffusive damping. The ray tracing is performed using background temperature and wind data obtained from MSISE-90 and HWM-07 models, respectively. For the Gadanki region, the suitability of these models is tested. Further, a climatological model of the background atmosphere for the Gadanki region has been developed using nearly 30 years of observations available from a variety of ground-based (MST radar, radiosonde, MF radar), rocket-, and satellite-borne measurements. ERA-Interim products are utilized for constructing background parameters corresponding to the meteorological conditions of the observations. By the reverse ray tracing method, the source locations for nine wave events could be identified to be in the upper troposphere, whereas, for five other events the waves got terminated in the mesosphere itself. Uncertainty in locating the terminal points of wave events in the horizontal direction is estimated to be within 50-100 km and 150-300 km for Gadanki and Hyderabad wave events, respectively. This uncertainty arises mainly due to non-consideration of the day-to-day variability in the tidal amplitudes. Prevailing conditions at the terminal points for each of the 14 events are provided. As no convection in-and-around the terminal points is noticed, convection is unlikely to be the source. Interestingly, large (~9 m/s/km) vertical shears in the horizontal wind are noticed near the ray terminal points (at 10-12 km altitude) and are thus identified to be the source for generating the observed high phase speed, high-frequency gravity waves.

Key words: Gravity wave sources, reverse ray tracing, wave action, airglow, model outputs.

1. Introduction

Atmospheric gravity waves (GWs) play an important role in the middle atmospheric structure and dynamics. They transport energy and momentum from the source region (mainly troposphere) to the upper atmosphere. The waves are dissipated on encountering critical level, transferring energy and momentum to the mean flow and leading to changes in the thermal structure of the atmosphere (Fritts and Alexander 2003). Several sources are identified for the generation of GWs, which include deep convection, orographic effect, vertical shear of horizontal wind and geostrophic adjustment. For GW generation from deep convection, mainly three mechanisms are considered (Fritts and Alexander 2003). These are (i) pure thermal forcing (e.g. Salby and Garcia 1987; Alexander et al., 1995; Piani et al., 2000; Fritts and Alexander 2003; Fritts et al., 2006), (ii) mechanical oscillator effect (e.g. Clark et al., 1986; Fovell et al., 1992), (iii) obstacle effect (e.g. Clark et al., 1986; Pfister et al., 1993; Vincent and Alexander 2000). The importance of these depends upon the vertical profile of local shear and time dependence of latent heat release. GWs from the convection source can have a wide range of phase speeds, frequencies and wavelengths unlike those from orography, which are generally confined to low ground-based frequencies and phase speeds (e.g. Queney., 1948; Lilly and Kennedy 1973; Nastrom and Fritts 1992; Eckermann and Preusse 1999; Alexander et al., 2010). In the shear excitation mechanism, mainly two processes, namely, sub-harmonic interaction and envelope radiation (Fritts and Alexander 2003) are considered. The latter process can yield horizontal scales of a few tens of km and phase speeds comparable to the mean wind. The geostrophic adjustment source is effective mainly in high latitudes (e.g. O'Sullivan and Dunkerton 1995; Shin Suzuki et al., 2013; Plugonven and Zhang 2014).

In general, significant progress has been made in the understanding of the physical processes leading to the spectrum of GWs through both observations and modeling. However, identification of the exact sources for the generation of GWs and their parameterization in the models remains a challenge (Geller et al., 2013). In order to identify the gravity wave sources, hodograph analysis has been widely used. Hodograph analysis can be used to identify the gravity wave parameters and which can be used as input parameters to the ray tracing. Using the hodograph, the direction of propagation of the wave and hence the location of the source can be ascertained. However, this method is applicable only for medium and low-frequency waves, as for the high frequency GWs the hodograph will not be an ellipse but nearly a straight line. Further, as it assumes monochromatic waves, it is not always applicable in the real atmosphere. Notwithstanding this limitation, using this method, convection and vertical shear have been identified as the possible sources of the observed medium and low-frequency GWs in the troposphere and lower stratosphere over many places (e.g., Venkat Ratnam et al., 2008). It becomes difficult to apply this method for GWs that are observed in the MLT region where simultaneous measurements of temperatures (with wind) would not be available.

A more appropriate method in such cases is ray tracing (Marks and Eckermann 1995), which is widely being used to identify the sources of GWs observed at mesospheric altitudes. Several studies (Hecht et al., 1994; Taylor et al., 1997; Nakamura et al., 2003; Gerrard et al., 2004; Brown et al., 2004; Wrasse et al., 2006; Vadas et al., 2009 and references therein) have been carried out to identify the sources for the GWs observed in the mesosphere using airglow images and in the stratosphere using Radiosonde and Lidar data (Guest et al., 2000; Hertzog et al., 2001). In mesospheric studies, important GW parameters, such as, periodicities and horizontal wavelengths (and sometimes vertical wavelengths when two imagers are

simultaneously used) are directly derived. A major limitation to the ray tracing method is the non-availability of realistic information on the background atmosphere. This is difficult to obtain with the available suite of instrumentation rendering identification of the source of the waves. Nevertheless, possible errors involved in identifying the terminal point of the waves with and without realistic background atmosphere have been estimated (e.g., Wrasse et al., 2006; Vadas et al., 2009).

Over the Indian region, several studies (Venkat Ratnam et al., 2008 and references therein) have been carried out for extracting GW parameters using various instruments (MST radar, radiosonde, Lidar and satellite observations). In a few studies (Kumar 2006., 2007; Dhaka et al., 2002; Venkat Ratnam et al., 2008; Debashis Nath et al., 2009; Dutta et al., 2009; Leena et al., 2012a, b) possible sources in the troposphere for their generation are identified which include convection, wind shear and topography.

In the present investigation, reverse ray tracing method is implemented to identify the sources of the GWs at mesospheric altitudes observed from an airglow imager located at Gadanki (13.5^{o}N, 79.2^{o}E) and from a balloon experiment which carried an ultraviolet imaging spectrograph from Hyderabad (17.5^{o}N, 78.5^{o}E). Wave amplitudes are also traced back including both radiative and diffusive damping. In Section 2 we described the instrumentation, in Section 3 the theory behind ray tracing, in Section 4 the background atmosphere used for ray tracing, in Section 5 application of the ray tracing method and in Section 6 identification of the sources of the observed waves.

2. Database

2.1. Airglow imager observations at Gadanki and methodology for extracting GW characteristics

The NARL Airglow Imager (NAI) located at Gadanki is equipped with a 24 mm Mamiya fish eye lens. It can monitor OH, O(^{1}S), and O(^{1}D) emissions and has a 1024x1024 pixel CCD as the detector, and a field-of-view of NAI is 90^o avoiding non-linearity arising at higher zenith angles. In the present study, only observations of O(^{1}S) emission which originate at ~93-100 km (with a peak emission altitude of ~97 km) are used. The exposure time used to measure the intensities of emissions was 70 s. After capturing the image, it has been analyzed and corrected for the background brightness, star brightness and actual coordinates. The area covered in the image is 200 km x 200 km with spatial resolution of 0.76 km near zenith and 0.79 km at the edges. More details of the NAI are discussed by Taori et al. (2013).

We have observed three wave events between 14:29-14:51 UTC, 15:44-15:50 UTC and 20:45-21:17 UTC on 17 March 2012 (Figure 1) and two-wave events between 15:47 - 16:27 UTC and 16:31 - 16:54 UTC on 19 March 2012 in the O(^{1}S) airglow emission intensities. In these images, crests of the waves are emphasized by yellow freehand lines and motion of the waves are apparent in the successive images shown one below the other. Red arrows indicate the direction of the propagation of the waves. Horizontal wavelengths of the GWs are determined by applying 2D FFT to the observed airglow images. The periods of the GWs are estimated by applying 1D FFT in time to the complex 2D FFT in space. Direction of propagation and phase speed of GWs are identified using successive images. More details of the methodology for estimating the GW parameters from NAI observations are provided in Taori et al. (2013). Table 1 summarizes the GW parameters extracted from the five wave events (G1 to G5) mentioned above. In general, the waves corresponding to these events are moving north, north-west direction. Zonal (k) and meridional (l) wave numbers are calculated using the relations $k = k_h \cos\phi$ and $l = k_h \sin\phi$ where k_h is the horizontal wave number and ϕ is the horizontal

direction of propagation observed from the airglow imager. The vertical wavelengths are calculated using the GW dispersion relation

$$\omega_{ir}^2 = \frac{N^2(k^2+l^2)+f^2(m^2+\alpha^2)}{k^2+l^2+m^2+\alpha^2} \qquad (1)$$

where ω_{ir} is the intrinsic frequency of the wave, N is the Brunt- Väiäsälä frequency, *f* is the Coriolis frequency and m is the vertical wave number. Zonal, meridional and vertical wavelengths can be derived from the parameters given in Table 1. The background atmosphere used for ray tracing is developed using 30 years of observations from various sources and will be discussed more in Section 4.

2.2. Daytime GW observations at Hyderabad obtained through optical emissions

A multi-wavelength imaging echelle spectrograph (MISE) is used to obtain daytime emission intensities of oxygen emissions at 557.7 nm, 630.0 nm and 777.4 nm in the MLT region at Hyderabad. MISE obtains high-resolution spectra of daytime skies which are compared with the reference solar spectrum. The difference obtained between the two yields information on the airglow emissions. The details of the emission extraction process and calibration procedures of the emission intensities and the salient results obtained in terms of wave coupling of atmospheric regions demonstrating the capability of this technique have been described elsewhere (Pallamraju et al., 2013; Laskar et al., 2013). In the present experiment, the slit oriented along the magnetic meridian enabled information on the meridional scale size of waves (λ_y) at O(^{1}S) emission altitude of ~ 100 km (in the daytime). An ultraviolet imaging spectrograph with its slit oriented in the east-west direction was flown on a high-altitude balloon (on 8 March 2010) which provided information on the zonal scale sizes of waves (λ_x) using the OI 297.2 nm emissions that originate at ~ 120 km. Both MISE and UVIS are slit spectrographs with array detectors providing 2-D information with one direction yielding high spectral resolution spectrum

(0.012nm at 589.3nm and 0.2nm at 297.2nm for MISE and UVIS, respectively), and the orthogonal direction yielding information on the dynamics over 330km (in the y-direction for OI 557.7nm emission) and 170km (in the x-directions for the OI 297.2nm emission). The spatial resolutions of these measurements are around 50km and 11km, respectively. The details of the experiment and the wave characteristics in terms of λ_x, λ_y, λ_H (horizontal scale sizes), time periods (τ), propagation speeds (c_H) and propagation direction (θ_H) obtained by this instrument at a representative altitude of 100 km are described in detail in Pallamraju et al. (2014). Nine events from this experiment which occurred on 8 March 2010 are considered in the present study for investigating their source regions and are marked as H1 to H9 in Table 1. All wave events observed at Gadanki and Hyderabad correspond to high frequency, high phase speed gravity waves as seen from their large vertical wavelengths, small periods and high phase speeds (Table 1).

2.3. Outgoing Long-wave Radiation (OLR) and Brightness Temperature in the Infrared band (IR BT)

Satellite data of OLR / IR BT are used as a proxy for tropical deep convection. In general, the daily NOAA interpolated OLR can be used to obtain information on the synoptic scale convection. However, for local convection on smaller spatial and temporal scales, the IR BT data merged from all available geostationary satellites (GOES-8/10, METEOSAT-7/5 GMS) are obtained from Climate Prediction Center, National Centre for Environment Prediction (NCEP) (source: ffp://disc2.nascom.nasa.gov/data/s4pa/TRMM_ANCILLARY/MERG/). The merged IR BT with a pixel resolution of 4 km is available for 60^oN to 60^oS (geo-stationary). The data in the East-West begins from 0.082^o E with grid increment of 0.03637^o of longitude and that in the North-South from 59.982^o N with grid increment of 0.03638^o of latitude (Janowiak et al.,

179 2001). The BT dataset is retrieved for every half an hour interval over regions of ±5° around
180 Gadanki and Hyderabad on 17 March 2012 and 8 March 2010, respectively, to see whether any
181 convective sources were present in these locations. Since the waves under study are high-
182 frequency waves propagating at high phase speeds with smaller horizontal wavelengths, a
183 maximum of 5^oX5^o grid is considered to be adequate. In general, the regions with OLR < 240
184 W/m^2 are treated as convective areas.

185 **3. Reverse ray tracing method**

186 We followed the treatment of ray tracing given by Marks and Eckermann (1995). Note
187 that the ray tracing theory is applicable only when WKB approximation is valid. When the WKB
188 parameter δ given by

189 $$\delta = \frac{1}{m^2}\left|\frac{\partial m}{\partial z}\right| \approx \left|\frac{1}{C_{gz}m^2}\frac{dm}{dt}\right| \qquad (2)$$

190 where C_{gz} is the vertical group velocity, m is the vertical wave number, t is the time and z
191 is the altitude, is less than unity, the approximation is taken to be valid.

192 In order to calculate the wave amplitude, we used the wave action equation of the form

193 $$\frac{\partial A}{\partial t} + \nabla.(C_g A) = -\frac{2A}{\tau} \qquad (3)$$

194 where $A = E/\omega_{ir}$ represents the wave action density, C_g represents the group velocity vector and

195 $E = \frac{\rho_0}{2}[\overline{u'^2} + \overline{v'^2} + \overline{w'^2} + N^2\overline{\zeta'^2}]$ represents the wave energy density being the sum of kinetic
196 and potential energy components, as described by wave perturbations in zonal, meridional and
197 vertical velocities (u', v', w'), and vertical displacement (ζ'). Here ρ_0 is the background density
198 and τ is the damping time scale (Marks and Eckermann, 1995). Using the peak horizontal

velocity amplitude along the horizontal wave vector we can calculate the wave action density using the equation:

$$A = \frac{1}{4}\frac{\rho_0 |\hat{u}_{\backslash\backslash}|^2}{\omega_{ir}}\{1+\frac{f^2}{\omega_{ir}^2}+\frac{N^2+\omega_{ir}^2}{N^2-\omega_{ir}^2}(1-\frac{f^2}{\omega_{ir}^2})\} \quad (4)$$

In order to avoid spatial integration in the wave action equation we can write Equation (3) in terms of the vertical flux of wave action $F = C_{gz} A$, where F is the vertical flux of wave action and C_{gz} is vertical component of the group velocity. Assuming negligible contribution from higher order terms, Equation (4) can be written as:

$$\frac{dF}{dt} = -\frac{2}{\tau}F \quad (5)$$

As the wave moves through the atmosphere, amplitude damping takes place which is mainly due to eddy diffusion and infrared radiative cooling by CO_2 and O_3. At higher altitudes (above about 100 km) molecular diffusion becomes important as compared to the eddy diffusion. We can calculate the damping rate due to diffusion using:

$$\tau_D^{-1} = D(k^2 + l^2 + m^2 + \alpha^2) \quad (6)$$

Where, $D = D_{Eddy} + D_{molecular}$, represents the sum of eddy and molecular diffusivities. Details of the calculation of D are given in the next section. In order to calculate the infrared radiative damping from 20-100 km we used the damping rate calculation method given by Zhu (1993). The total damping rate is calculated using the following equation:

$$\tau^{-1} = \frac{\tau_r^{-1}\left(\frac{1-f^2/\omega_{ir}^2}{1-\omega_{ir}^2/N^2}\right) + \tau_D^{-1}\left(1+\frac{f^2}{\omega_{ir}^2}+\frac{1-f^2/\omega_{ir}^2}{N^2/\omega_{ir}^2-1}+\mathrm{Pr}^{-1}\frac{1-f^2/\omega_{ir}^2}{1-\omega_{ir}^2/N^2}\right)}{\left\{1+\frac{f^2}{\omega_{ir}^2}+\frac{N^2+\omega_{ir}^2}{N^2-\omega_{ir}^2}\left(1-\frac{f^2}{\omega_{ir}^2}\right)\right\}} \quad (7)$$

Where Pr is prandtl number. Note that for high-frequency waves diffusion damping effect will be less.

4. Background atmosphere

In order to carry out reverse ray-tracing, information on background atmospheric parameters (U, V and T) is required right from the initial point (mesosphere) to the termination point (frequently in the troposphere). In general, there is no single instrument which can probe the troposphere, stratosphere, and mesosphere simultaneously. Note that in order to trace the ray we require atmospheric parameters for a specified latitude-longitude grid. Since the observed wave events belong to high frequencies (GWs with short horizontal wavelengths and high vertical wavelengths), we require the background information at least for grid sizes of 5^o x 5^o around Gadanki and Hyderabad. For the information on temperature and density at the required grids, we used Extended Mass Spectrometer and Incoherent Scatter Empirical Model (MSISE-90) data (Hedin, 1991) from surface to 100 km with an altitude resolution of 0.1 km for 0.1^ox0.1^o grid around these locations. Note that the MSISE-90 model is an empirical model which provides temperature and density data from the surface to the thermosphere. For horizontal winds at the required grids, we used the outputs from the Horizontal Wind Model (HWM-07) (Drob et al., 2008) data. This model has been developed by using a total of 60 x 10^6 observations available from 35 different instruments spanning 50 years. Further, long-term data available from a variety of instruments (MST radar, MF radar, Rocketsonde, radiosonde, HRDI /UARS and

236 SABER/TIMED satellites) in-and-around (±5 degree) Gadanki have been used to develop a
237 background climatological model profiles of U, V, and T on monthly basis. Details of the data
238 used to develop the background temperature and horizontal winds are provided in Table 2.
239 Monthly mean contours of temperature, zonal and meridional winds obtained from the
240 climatological model (from now on referred to as the Gadanki model) are shown in Figure 2. In
241 general, significant features of the background atmospheric structure for a typical tropical region
242 can be noticed from this figure. Tropopause, stratopause, and mesopause altitudes are located at
243 around 16-18 km, 48-52 km, and 98-100 km with temperatures 190-200 K, 260-270 K and 160-
244 170 K, respectively. Mesospheric semi-annual oscillation around 80-85 km is also seen (Figure
245 2a). Tropical easterly jet at around 16 km during the Indian Summer Monsoon season (June-
246 July-August) and semi-annual oscillation near the stratopause (and at 80 km with different
247 phase) are also clearly visible in the zonal wind (Figure 2b). Meridional winds do not exhibit any
248 significant seasonal variation in the troposphere and stratosphere but show large variability in the
249 mesosphere (Figure 2c). These overall features in the background temperature and wind match
250 well with those reported considering data from different instruments by Kishore Kumar et al.,
251 (2008a,b).

252 The profiles of T obtained from MSISE-90 model and U and V from HWM-07 for 17
253 March 2012 are shown in Figure 3(a)-(c), respectively. The Gadanki model mean temperature
254 profile for the month of March and the temperature profile obtained from TIMED/SABER and
255 mean temperature obtained from ERA-Interim for the month of March 2012 are also
256 superimposed in Figure 3a for comparison. A very good agreement between the profiles can be
257 noticed. The profiles of U and V obtained from the Gadanki model for the month of March and
258 also the monthly mean of the ERA-Interim are also superimposed in Figure 3b and 3c,

259 respectively. In general, a good match is seen between the Gadanki model and ERA-Interim and
260 HWM-07 models up to the altitude of the stratopause. The differences between the two above the
261 stratopause could be due to tidal winds which have large amplitudes at mesospheric altitudes.
262 Though tidal amplitudes are already included in the HWM-07 model, their day-to-day variability
263 may be contributing to these differences. In order to avoid any bias due to day-to-day variability
264 of the tides at mesospheric altitudes, we have considered tidal amplitudes of 5 K, 10 K, 15 K and
265 10 m/s, 20 m/s, 30 m/s in temperature and winds, respectively, at 97 km to represent day-to-day
266 variability.

267 In general, troposphere is a highly dynamic region though the amplitudes of tides are
268 considerably small. In order to consider more realistic horizontal winds in the troposphere and
269 stratosphere, we further considered the ERA-Interim products (Dee et al., 2011). This data is
270 available at 6 h intervals with 1.5^0 x 1.5^0 grid resolution at 37 pressure levels covering from
271 surface (1000 hpa) to the stratopause (~1 hPa). The profiles of T, U and V from ERA-Interim for
272 17 March 2012 for 12 UTC are also superimposed in Figures 3(a), 3(b) and 3(c), respectively. In
273 general, good agreement between the other models and ERA-Interim model can be noticed
274 particularly in V in the lower and upper levels except between 10 and 20 km. Summarizing, we
275 have considered the following wind models: (1) ERA-Interim (from surface to 40 km) and HWM
276 07 models from 40-100 km, (2) Gadanki model, (3) zero wind (U=0 and V=0). Using these
277 background atmosphere profiles, we calculated the relevant atmospheric parameters like N^2 and
278 H. Profiles of T, U, and V obtained using ERA-interim data products for 8 March 2010, 6 UTC
279 over Hyderabad region are shown in Figures 3(c)-(f), respectively. T, U, and V profiles as
280 obtained from MSISE-90 and HWM-07 for the same day are also provided in the respective

281 panels. The background atmosphere information for wave events over Hyderabad is obtained in a
282 manner similar to that mentioned above for Gadanki.

283 In order to calculate diffusive damping we used eddy diffusivity profiles for troposphere
284 and lower stratosphere and mesosphere which are obtained using MST Radar (Narayana Rao et
285 al., 2001) at Gadanki as shown in Figure 4a. In the altitude regions where there are data gaps, we
286 extrapolated/interpolated the diffusivity profiles and the approximated profile with different
287 analytical exponential functions are also shown in Figure 4a. The eddy diffusivity profile of
288 Hocking (Hocking, 1991) that is presented in Marks and Eckermann (1995) is also superimposed
289 for comparison. Note that Hocking's profile corresponds mainly to mid-latitudes. In general,
290 eddy diffusivity is relatively higher in Hocking's profile than in the Gadanki profile. This same
291 (Gadanki) profile is used for Hyderabad events also. In Figure 4b molecular diffusivity is shown.
292 It is seen that the molecular diffusivity exceeds the eddy diffusivity at altitudes > 80 km. We
293 have taken into account molecular diffusivity also in the ray tracing calculation while
294 considering the total diffusivity above 80 km and the total diffusivity profile is shown in Figure
295 4b. Radiative and diffusive damping rates corresponding to Event G1 observed over Gadanki are
296 shown in Figure 4c for illustration. It is seen that radiative damping rate is higher than the
297 diffusive damping rate below 95 km. This is so for the other 13 events (G2-G5 and H1-H9) as
298 well.

299 **5. Application of reverse ray tracing for the wave events**

300 By using the background parameters and the ray tracing equations, we trace back the ray
301 path(s) to identify the GW source region(s). We used Runge-Kutta fourth order method for
302 numerical integration at the time step of $\delta t = 100 \text{ m}/C_{gz}$ where 100 m is the height step
303 downwards from 97 km (the peak altitude of the airglow layer) and C_{gz} is the vertical group

304 velocity. As the ray tracing treatment is valid only when WKB approximation holds good, the
305 ray integration is terminated whenever the WKB approximation is violated. We terminated the
306 ray 1) when m^2 becomes negative, which means that the wave cannot propagate vertically, 2)
307 when intrinsic frequency is < 0 or approaching zero, which means that the wave reached a
308 critical layer and is likely to break beyond this 3) when the WKB parameter is approaching
309 values greater than one (beyond which WKB approximation breaks) and 4) when vertical wave
310 number is becoming greater than 1 $x10^{-6}$ (approaching critical level) (Wrasse et al., 2006). We
311 calculated the wave action and thus the amplitude along the ray path by including the damping.
312 As the information on wave amplitudes cannot be unambiguously determined from the optical
313 emission intensity measurements, we assumed the GW amplitude as unity (at 97 km) and traced
314 back the relative amplitudes along the ray path. Further, as we have not considered the local time
315 variation of the background parameters, the ground-based wave frequency will be a constant.
316 However, note that the intrinsic frequency still varies with altitude because of the varying
317 background horizontal winds.

318 The observed and calculated GW parameters (intrinsic frequency, wave period, zonal,
319 meridional, and vertical wave numbers) for all the wave events measured at the peak airglow
320 emission altitudes as described in Sections 2.1 and 2.2 are given as initial parameters to the ray
321 tracing code. We considered all the different combinations of observed wave parameters
322 including the errors in the observations for obtaining the ray paths and the uncertainties in them.
323 Note that atmospheric tides have large amplitudes in the MLT region which, at times, can be
324 comparable to those of the background wind. As mentioned earlier, though tidal amplitudes are
325 considered in the HWM-07 model, their day-to-day variability is not taken into account in the
326 model. Amplitudes of the tides may reach values as high as 20 m/s over equatorial latitudes

(Tsuda et al., 1999). As already mentioned we have included day to day variability of tidal amplitudes into temperature and winds. In general, above the stratopause, tidal amplitudes are large and increase exponentially with altitude. It is interesting to note that (figure not shown) the variability in the background atmospheric parameters developed using data from a suite of instruments as mentioned above lies within the variability due to tides. Ray path calculations are also carried out for these background profiles.

We traced the ray path using the above initial parameters from the initial latitude (13.5^{o}N/17.5^{o}N) and longitude (79.2^{o}E/78.5^{o}E) and altitude (97 km). The ray paths for the wave event G1 with the longitude-altitude, latitude-altitude and longitude-latitude are shown in Figures 5(a)-(c), respectively, for Gadanki and in Figures 5 (d)-(f) for (H1) Hyderabad. Ray paths obtained while considering different background conditions (normal wind, zero wind and Gadanki model wind) and the day-to-day variability of tides are also superimposed with dotted lines. When we considered zero (Gadanki) wind, a shift of 71 km (25 km) in the horizontal position of the terminal point is observed with respect to that for normal wind for wave event G1. The shift reduced to 19 km and increased to 47 km and 97 km when we considered the tidal variability of +5K, +10 m/s and +10 K, +20 m/s, +15 K, +30 m/s, respectively, with respect to the normal wind. The shift is ~15 km for the tidal variability of -5 K, -10 m/s. The ray terminated in the mesosphere itself for tidal variability of -10 K, -20 m/s and -15 K, -30 m/s (figure not shown).

Over Hyderabad, for the wave event H1, shown in Figures 5(d)-(f), the shifts in the horizontal location of the terminal point are 305.6 km (148.7 km) for tidal variability of +10, +20 m/s (-10 K, -20 m/s), respectively, with reference to zero wind. This difference is only 59.5 km for tidal variability of -10 K, -20 m/s with respect to the normal wind. The terminal point

350 locations for the rest of the wave events for normal winds are listed in Table 1. Note that out of
351 the five wave events over Gadanki two wave events (G3 and G4) got terminated in the upper
352 mesosphere itself and one (G5) got terminated at 67 km. Over Hyderabad, out of the nine wave
353 events, two wave events (H4 and H7) got terminated at ~ 67 km. In general, all the wave events
354 which propagated down to the upper troposphere terminated between 10 and 14.5 km, except the
355 case G2 which got terminated at 17 km due to violation of the WKB approximation. The
356 violation of the WKB approximation at 17 km could be due to sharp temperature gradients near
357 tropopause.

358 Profiles of square of vertical wave number (m^2), intrinsic frequency (ω_{ir}) and Brunt
359 Väiäsälä frequency (N), horizontal wavelength (λ_h), zonal, meridional, and vertical group speed
360 for the event G1 are shown in Figures 6(a)-(f), respectively. Profiles of these parameters obtained
361 for different background wind conditions (normal wind, zero wind, and Gadanki model wind)
362 and the day-to-day variability of tides are also superimposed in the respective panels. The
363 differences with and without the variability of tides in the parameters mentioned above are small
364 below the stratopause, and are quite high above. Note that the effect of Doppler shifting of the
365 wave frequency is larger at higher altitudes due to higher wind amplitudes. Around 13 km, Brunt
366 Väisälä frequency is less than that of the intrinsic frequency and so the square of the vertical
367 wave number is negative there (Figure 6b). The variation in the horizontal wavelength with
368 height (Figure 6c) is small. Zonal group speed shows (Figure 6d) nearly the same behaviour as
369 that of the zonal wind. The intrinsic frequency, $\omega_{ir,}$ exceeded N at 13 km altitude and due to this
370 m^2 became negative and the ray path got terminated there. The observation time at the ray-start
371 and the times along the ray time shown in Figure 6(a) reveal that it has taken 63 minutes for the
372 ray propagation.

373 As mentioned earlier, the information on the wave amplitudes is not available from the
374 observations. So we used the GW amplitude as unity (at the altitude of observation) and traced
375 back the relative amplitudes along the ray path. Profiles of amplitudes of GWs observed for the
376 wave events G1 and H1 over Gadanki and Hyderabad are shown in Figures 7(a) and 7(b),
377 respectively. Amplitudes with three different background wind conditions along with different
378 tidal amplitudes are also shown in the respective panels. Unity wave amplitude at the observed
379 region, translates to an amplitude of 10^{-3} near the source region. Amplitude growth is found
380 higher when either Gadanki or zero wind models are considered and slightly lower for the
381 normal wind. The growth is highly reduced when tidal variability in the background wind is
382 considered. However, higher amplitude growth rates are obtained over Hyderabad when we
383 considered normal wind along with tidal variability than zero wind. Similar growth rates are also
384 obtained for other wave events (not shown). Thus, background winds play an important role in
385 the growth rates of GWs.

386 **6. Discussion on the potential source(s) of the GW events**

387 The geographical locations of the terminal points for different combinations of
388 background winds along with different combinations of tidal variability are shown in Figures 8
389 and 9 for Gadanki and Hyderabad wave events, respectively. In these figures, the contour
390 encircling all the points (not drawn in the panels of the figure) represents the horizontal spread of
391 uncertainty due to background conditions (including tidal variability). Terminal point of the ray
392 (in the troposphere) is expected to be the location of GW source. Since 9 out of 14 wave events
393 got terminated between 10 and 17 km, we search for the possible sources around this altitude at
394 the location.

In general, primary sources for the GW generation over tropics are orography, convection, and vertical shear in the horizontal winds. In the present case, GWs are unlikely to be the orographic origin as the observed waves have phase speeds are much greater than zero. Tropical deep convection is assumed to be a primary source for the generation of wide spectrum of GWs in the tropical latitudes. As mentioned earlier, OLR/IR BT is considered to be the proxy for the tropical deep convection. Lower the OLR/BT values, higher the cloud top and hence deeper the convection. OLR (IRBT) < 240 W/m^2 (K) is taken to represent deep convection. However, convection may exist at locations away from the observational site and waves generated at those locations can propagate to the mesospheric altitudes over the site. In order to see the presence or otherwise of convection in the vicinity of the termination location, latitude-longitude cross section of NOAA interpolated OLR obtained for 17 March 2012 (8 March 2010) is shown in Figure 8a (Figure 9a) for Gadanki (Hyderabad) region. The terminal points of the rays for the wave events G1 and G2 (H1-H9 except H4 and H7) with different background wind conditions and different combinations of variability of the tides are also shown in the figure. There is no convection in-and-around Gadanki (Hyderabad) region as can be noticed from this figure. Note that this plot is with a coarse grid (2.5^o x 2.5^o latitude-longitude) averaged for a day. The observed GWs could be generated due to localized sources having shorter temporal and spatial scales than those seen from the NOAA OLR data used. In order to examine this, we have used IR BT data which is available at 4 km x 4 km grid size and at half an hour basis. Latitude and longitude section of hourly IR BT at 14 UTC (10 UTC), 15 UTC and 16 UTC is shown in Figures 8(b)-(d) (Figure 9b), respectively. The terminal points with and without variability of the tides are also shown. Interestingly no cloud patches are seen at any of the times mentioned above. Thus, convection can be ruled out as a possible source for the observed wave events.

418 The other possible source for GW generation is the vertical shear of the horizontal wind.
419 The vertical shear in horizontal winds at an altitude of 10 km (8 km) on 17 March 2012 (8 March
420 2010) as a function of latitude-longitude is shown in Figure 10a (Figure 10b). The terminal
421 points of the rays for both the wave events with and without the day-to-day variability of the
422 tides are also shown in the figure. Interestingly, at all the terminal points (in the troposphere),
423 strong vertical shear in the horizontal wind which is quite high (8-9 m/s/km) is seen. In order to
424 see whether these waves could be generated due to non-linear interaction (through Kelvin
425 Helmholtz Instability, KHI), the Richardson number ($Ri = \frac{N^2}{(dU/dz)^2}$) for the nearest location
426 is calculated (using nearby radiosonde data) and is shown in Figure 11. From the figure it can be
427 noticed that Ri is < 0.25 showing that Ri satisfies the condition for instability for the observed
428 waves at both the stations. Thus, the shear is unstable and hence conducive for the excitation of
429 KHI leading to the generation of the propagating GWs through non-linear interaction. Note that
430 shear excitation of the GWs has been examined theoretically using both linear and non-linear
431 approaches (e.g., Fritts, 1982; 1984; McIntyre, 1978). For the excitation of radiating GWs by KH
432 instabilities at a shear layer, the two mechanisms that are examined are the vortex pairing (sub-
433 harmonic interaction) and envelope radiation (Fritts, 1984). The vortex pairing is found to be
434 highly dependent on the minimum Ri, whereas, the envelope radiation mechanism is found to
435 provide efficient radiating wave excitation in the absence of propagating unstable modes (Fritts,
436 1984). Theoretical and numerical simulation work needs to be carried out to examine which of
437 these mechanisms is adequate for the observed events in the present study. This aspect is beyond
438 the scope of the present study and is planned to be taken up in the future.
439 Note that five wave events terminated at mesospheric altitudes. We examined the
440 background atmospheric condition which can lead to the termination of these wave events at

such high altitudes. The ray paths for two wave events observed on the same day over Gadanki could propagate down below with the same background atmosphere. When wave parameters related to this event are examined (Table 1), it can be seen that the phase speeds are small when compared to the other two wave events. When the wave is introduced at around 15 km with all the wave parameters similar to that observed at 97 km for this event and forward ray tracing is carried out, it is seen that the ray propagated up to 50 km terminating there. Note that strong vertical shear in the background wind is seen at this altitude (Fig. 3). To investigate the role of shear in the process of propagation of waves, the shear is reduced to almost 0 in the 50 – 80 km altitude region. Under such conditions this wave event also could propagate to ~16 km in the reverse ray tracing. This reveals that the background wind shear is obstructing the ray path. It is quite likely that the wave got ducted between 50 and 80 km and similar results are obtained for the other cases which got terminated in the mesosphere. This indicates that wind shears at mesospheric altitudes are responsible for termination at mesospheric altitudes for these events.

7. Summary and Conclusions

Identification of the GW sources for the 14 wave events observed over Gadanki and Hyderabad using optical airglow measurements is presented. Reverse ray tracing method is developed to obtain the location of the source regions of the GWs in the troposphere/mesosphere. We made use of the MSISE-90 model for temperature and the HWM-07 for the zonal and meridional winds in addition to the ERA-Interim products in the lower atmosphere (1000 hPa to 1 hPa pressure levels), Gadanki climatological model and zero wind model for the background atmosphere. We have incorporated also the expected variability of tidal amplitudes of 5 K, 10 K, 15 K and 10 m/s, 20 m/s, 30 m/s in temperature and winds, respectively. The terminal points lie in the range of 50-100 km and 60-300 km for Gadanki and

464 Hyderabad, respectively when different wind and tidal variabilities are used. Wave action is
465 implemented taking into account the radiative and diffusive damping. Considering the wave
466 amplitude as unity at 97 km, amplitude of the wave is traced back to the source region for
467 different wind models. Out of the 14 events examined, 9 ray paths terminated in the troposphere.
468 The remaining 5 events got terminated in the mesosphere itself. We examined for possible
469 sources for the 9 events for which the ray paths terminated in the troposphere.

470 Orography as the possible source was ruled out as wave events have high phase speeds.
471 No tropical deep convection in-and-around Gadanki and Hyderabad was noticed near the ray
472 terminal points. Interestingly, strong vertical shear in the horizontal wind is observed near the
473 terminal points, and these large shears are attributed to be the source for the GW events observed
474 at the mesospheric altitudes. Preusse et al., (2008) discussed the transparency of the waves to the
475 atmosphere in different seasons. They reported that during equinox times atmosphere is more
476 transparent to the high phase speed and shorter horizontal wavelength waves than that in the
477 solstices. Waves with shorter (<10 km) horizontal wavelengths tend to be removed by vertical
478 reflection or evanescence at the source, and a slower phase speeds are more prone to the critical
479 level removal. This leads to a preference for waves with longer horizontal wavelengths and a
480 faster ground-based phase speeds to reach the MLT. However, they observed that many rays
481 penetrated to the MLT at the tropical latitude where wind speed is low in comparison to the mid
482 and high latitudes. In our case, whenever phase speed is low for short horizontal wavelength
483 waves, the wave did not reach up to the troposphere and it got stopped at mesospheric altitude
484 itself. While there is strong evidence for convectively generated gravity waves, evidence for
485 tropospheric wind shear generated GWs is rather sparse (Mastrantonio 1976; Fritts and
486 Alexander 2003). The present study clearly demonstrated that high-frequency high phase speed

GWs observed in the mesosphere can be generated by tropospheric wind shear. Examination of the background wind conditions and wave parameters for the events that got terminated in the mesosphere revealed that the phase speeds were quite small for these strong vertical shears in the 50-80 km region (and at 95 km) resulting in termination of the ray paths. A potential explanation is that the waves generated in the troposphere are ducted between 50-80 km and the waves observed above this region are due to leakage of waves from the duct. It is also likely that the observed GWs in these cases (G3,G4,G5,H5 and H7) are from secondary wave generation due to wave breaking at the termination region. While secondary wave generation due to convectively generated waves has been investigated (e.g. Zhou et al., 2002; Chun and Kim 2008) such investigations have not yet been carried out for GWs of shear origin. This aspect needs further investigation. Note that we have tested reverse ray tracing method successfully for fourteen wave events. Further, wave action is also implemented successfully by assuming the wave amplitudes as unity as information on the same is not available from optical observations. However, more number of cases are needed to be examined, particularly for the events that occur during Indian Summer Monsoon season where convection and strong vertical shears in the horizontal winds co-exist due to prevailing tropical easterly jet (Venkat Ratnam et al., 2008). A few experiments are planned to be conducted at Gadanki by operating simultaneously MST radar, Radiosonde, Rayleigh Lidar, Airglow imager and Meteor radar which provide information right from the troposphere to the MLT region. Note that such a study on the vertical propagation of meso-scale gravity wave from lower to upper atmosphere was made recently by Shin Suzuki et al. (2013) using Airglow Imager and Lidar over the Arctic region.

509 **Acknowledgments:** This work is done as a part of SAFAR and CAWSES India phase II
510 programs. We thank NARL staff for providing data used in the present study. We deeply
511 appreciate NOAA, HWM-07, ERA-Interim for providing data used in the present study through
512 their ftp sites. This work is supported by Department of Space, Government of India.
513

514 **References**

515 Alexander, M. J., J. R. Holton, and D. R. Durran (1995), The gravity wave response above deep
516 convection in a squall line simulation. J. Atmos. Sci., 52, 2212-2226.

517 Alexander , M. J., M. Geller, C. McLandress, S. Polavarapu, P. Preusse, F. Sassi, K. Sato, S.
518 Eckermann, M. Ern, A. Hertzog, Y. Kawatani, M. Pulido, T. A. Shaw, M.Sigmond, R. Vincent
519 and S. Watanabe (2010), Recent developments in gravity-wave effects in climate models, and
520 the global distribution of gravity-wave momentum flux from observations and models, Q. J. R.
521 Meteorol. Soc. 136: 1103–1124.

522 Brown, L. B., A. J. Gerrard, J. W. Meriwether, J. J. Makela (2004), All-sky imaging
523 observations of mesospheric fronts in OI 557.7 nm and broadband OH airglow emissions:
524 Analysis of frontal structure, atmospheric background conditions, and potential sourcing
525 mechanisms, J. Geophys. Res., 109, D19104, doi:10.1029/2003JD004223.

526 Chun, H.Y., Y.H. Kim (2008), Secondary waves generated by breaking of convective gravity
527 waves in the mesosphere and their influence in the wave momentum flux, J. Geophys. Res.,
528 113, D23107, doi:10.1029/2008JD009792, 2008.

529 Clark, T. L., T. Hauf, and J. P. Kuettner (1986), Convectively forced internal gravity waves:
530 Results from two-dimensional numerical experiments, Q. J. R. Meteorol. Soc., 112, 899– 925,
531 doi:10.1002/qj.49711247402.

532 Debashis Nath., M. Venkat Ratnam, V. V. M. Jagannadha Rao, B. V. Krishna Murthy, and S.
533 Vijaya Bhaskara Rao (2009), Gravity wave characteristics observed over a tropical station
534 using high-resolution GPS radiosonde soundings, J. Geophys. Res., 114, D06117,
535 doi:10.1029/2008JD011056.

536 Dee, D. P., S. M. Uppala, A. J. Simmons, P. Berrisford, P. Poli, S. Kobayashi, U. Andrae, M. A.

537 Balmaseda, G. Balsamo, P. Bauer, P. Bechtold, A. C. M. Beljaars, L. van de Berg, J. Bidlot, N.
538 Bormann, C. Delsol, R. Dragani, M. Fuentes, A. J. Geer, L. Haimberger, S. B. Healy, H.
539 Hersbach, E. V. Hólm, L. Isaksen, P. Kållberg, M. Köhler, M. Matricardi, A. P. McNally, B. M.
540 Monge-Sanz, J.-J. Morcrette, B. K. Park, C. Peubey, P. de Rosnay, C. Tavolato, J.-N. Thépaut
541 and F. Vitart (2011), The ERA-Interim-reanalysis: configuration and performance of the data
542 assimilation system, Q. J. R. Meteorol. Soc.137: 553 – 597.
543 Dhaka, S. K., R. K. Choudhary, S. Malik, Y. Shibagaki, M. D. Yamanaka, and S. Fukao (2002),
544 Observable signatures of a convectively generated wave field over the tropics using Indian
545 MST radar at Gadanki (13.5^{o}N, 79.2^{o}E), Geophys. Res. Lett., 29(18), 1872,
546 doi:10.1029/2002GL014745.
547 Drob, D.P., J. T. Emmert, G. Crowley, J. M. Picone, G. G. Shepherd, W. Skinner, P. Hays, R. J.
548 Niciejewski, M. Larsen, C. Y. She, J. W. Meriwether, G. Hernandez, M. J. Jarvis, D. P. Sipler,
549 C. A. Tepley,M. S. O'Brien, J. R. Bowman, Q. Wu, Y. Murayama, S. Kawamura, I. M. Reid
550 and R. A. Vincent (2008), An empirical model of the Earth's horizontal wind fields: HWM07,
551 J. Geophys. Res., 113, A12304, doi:10.1029/2008JA013668.
552 Dutta, G., M. C. Ajay Kumar, P. Vinay Kumar, M. Venkat Ratnam, M. Chandrashekar, Y.
553 Shibagaki, M. Salauddin, and H. A. Basha (2009), Characteristics of high-frequency gravity
554 waves generated by tropical deep convection: Case studies, J. Geophys. Res., 114, D18109,
555 doi:10.1029/2008JD011332.
556 Eckermann, S. D (1992), Ray-tracing simulation of the global propagation of inertia gravity
557 waves through the zonally averaged middle atmosphere. J. Geophys. Res., 97, 15,849-15,866.
558 Fovell, R., D. Durran, and J. R. Holton (1992), Numerical simulations of convectively generated
559 stratospheric gravity waves. J. Atmos. Sci., 49, 1427-1442.

560 Fritts, D.C (1982), Shear Excitation of Atmospheric Gravity Waves. J. Atmos. Sci., 39, 1936-
561 1952.
562 Fritts, D.C, (1984), Shear Excitation of Atmospheric Gravity Waves, Part II: Nonlinear
563 Radiation from a Free Shear Layer, J. Atmos. Sci., 41, 524-537.
564 Fritts, D.C., M.J. Alexander (2003), Gravity wave dynamics and effects in the middle
565 atmosphere. Reviews of Geophysics 41 (1), doi: 10.1029/2001RG000106.
566 Fritts, D.C., Sharon L. Vadas, Kam Wan, Joseph A. Werne (2006), Mean and variable forcing of
567 the middle atmosphere by gravity waves, J. Atmos. and Sol. Terr. Phys., 68, 247–265.
568 Geller, M.A., M.J. Alexander, P.T. Love, J. Bacmeister, M. Ern, A. Hertzog, E. Manzini, P.
569 Preusse, K. Sato, A. Scaife, and T. Zhou (2013), A comparison between gravity wave
570 momentum fluxes in observations and climate models. J. Climate, 26, 6383-6405,
571 doi:10.1175/JCLI-D-12-00545.1.
572 Gerrard, A.J., Timothy J. Kane, Stephen D. Eckermann, and Jeffrey P. Thayer (2004), Gravity
573 waves and mesospheric clouds in the summer middle atmosphere: A comparison of lidar
574 measurements and ray modeling of gravity waves over Sondrestrom, Greenland, J. Geophys.
575 Res., 109, D10103, doi:10.1029/2002JD002783.
576 Guest, F.M., M.J. Reeder, C.J. Marks, D.J. Karoly (2000),Inertia–Gravity Waves Observed in
577 the Lower Stratosphere over Macquarie Island, J. Atmos. Sci., 57.
578 Hecht, J.H., R.L. Walterscheid, M.N. Ross (1994), First measurements of the two-dimensional
579 horizontal wave number spectrum from CCD images of the nightglow. J. Geophys. Res., 99
580 (A6), 11449–11460.
581 Hedin, A.E (1991), Extension of the MSIS Thermosphere model into the middle and Lower
582 atmosphere, J. Geophys. Res., 96, NO. A2, 1159-117.

583 Hertzog, A., C. Souprayen, and A. Hauchecorne (2001), Observation and backward trajectory of
584 an inertio-gravity wave in the lower stratosphere, Annales Geophysicae., 19, 1141–1155.
585 Hocking, W.K., (1991), The effects of middle atmosphere turbulence on coupling between
586 atmospheric regions, J. Geomag., Geoelc., 43 (sup), 621-636.
587 Janowiak, J.E., R.J. Joyce, and Y. Yarosh (2001), A real-time global half-hourly pixel-resolution
588 IR dataset and its applications. Bull. Amer. Meteor. Soc., 82, 205-217.
589 Jones, W.L (1969), Ray tracing for internal gravity waves. J. Geophys. Res., 74 (8), 2028–2033.
590 Kumar, K. K. (2006), VHF radar observations of convectively generated gravity waves: Some
591 new insights, Geophys. Res. Lett., 33, L01815, doi:10.1029/2005GL024109.
592 Kumar, K. K. (2007), VHF radar investigations on the role of mechanical oscillator effect in
593 existing convectively generated gravity waves, Geophys. Res. Lett., 34, L01803,
594 doi:10.1029/2006GL027404.
595 Kishore Kumar, G., M. Venkat Ratnam, A. K. Patra, S. Vijaya Bhaskara Rao, and J. Russell
596 (2008a), Mean thermal structure of the low-latitude middle atmosphere studied using Gadanki
597 Rayleigh lidar, Rocket, and SABER/TIMED observations, J. Geophys. Res., 113, D23106,
598 doi:10.1029/2008JD010511.
599 Kishore Kumar, G., M. Venkat Ratnam, A. K. Patra, V. V. M. Jagannadha Rao, S. Vijaya
600 Bhaskar Rao, K. Kishore Kumar, S. Gurubaran, G. Ramkumar, and D. Narayana Rao (2008b),
601 Low-latitude mesospheric mean winds observed by Gadanki mesosphere-stratosphere-
602 troposphere (MST) radar and comparison with rocket, High Resolution Doppler Imager
603 (HRDI), and MF radar measurements and HWM93, J. Geophys. Res., 113, D19117,
604 doi:10.1029/2008JD009862.

605 Laskar, F. I., D. Pallamraju, T. Vijaya Lakshmi, M. Anji Reddy, B. M. Pathan, and S.
606 Chakrabarti (2013), Investigations on vertical coupling of atmospheric regions using combined
607 multiwavelength optical dayglow, magnetic, and radio measurements, J. Geophys. Res. Space
608 Physics, 118, 4618-4627, doi:10.1002/jgra.50426.
609 Leena, P.P., M. Venkat Ratnam, B.V. KrishnaMurthy, S.VijayaBhaskaraRao (2012a), Detection
610 of high frequency gravity waves using high resolution radiosonde observations, J. Atmos. Sol.
611 Terr. Phys., 77, 254–259.
612 Leena, P.P., M.Venkat Ratnam, B.V.Krishna Murthy (2012b), Inertia gravity wave
613 characteristics and associated fluxes observed using five years of radiosonde measurements
614 over a tropical station, J. Atmos. Sol. Terr. Phys., 84–85, 37–44.
615 Lilly, D. K., and P. J. Kennedy (1973), Observations of a stationary mountain wave and its
616 associated momentum flux and energy dissipation. J. Atmos. Sci., 30, 1135-1152.
617 Mastrantonio, G., F. Einaudi, D. Fua, and D. P. Lalas (1976), Generation of gravity waves by jet
618 streams in the at-mosphere, J. Atmos. Sci., 33, 1730-1738.
619 Marks, C.J., S.D. Eckermann (1995), A three-dimensional non-hydrostatic ray-tracing model for
620 gravity waves: formulation and preliminary results for the middle atmosphere. J. Atmos. Sci.,
621 52 (11), 1959–1984.
622 McIntyre, M.E., and M. A. Weissman (1978), On Radiating Instabilities and resonant over-
623 reflection. J. Atmos. Sci., 35, 1190-1196.
624 Nakamura, T., T. Aono, T. Tsuda, A.G. Admiranto, E. Achmad Suranto (2003), Mesospheric
625 gravity waves over a tropical convective region observed by OH airglow imaging in Indonesia.
626 Geophysical Research Letters 30 (17), 1882–1885.

627 Narayana Rao, D., M. V. Ratnam, T. N. Rao, S. V. B. Rao (2001), Seasonal variation of vertical
628 eddy diffusivity in the troposphere,lower stratosphere and mesosphere over a tropical station.
629 Annales Geophysicae , 19.
630 Nastrom, G.D., D.C. Fritts (1992), Sources of mesoscale variability of gravity waves I:
631 topographic excitation. J. Atmos. Sci., 49 (2), 101–110.
632 O'Sullivan,D., and T.J. Dunkerton (1995), Generation of Inertia Gravity waves in a simulated
633 life cycle of Baroclinic Instability, J. Atmos. Sci., 52(21).
634 Pallamraju, D., F. I. Laskar, R. P. Singh, J. Baumgardner, and S. Chakrabarti (2013), MISE: A
635 Multiwavelength Imaging Spectrograph using Echelle grating for daytime optical agronomy
636 investigations, J. Atmos. Sol-Terr. Phys., 103, 176 - 183.
637 Pallamraju, D., J. Baumgardner, R. P. Singh, F. I. Laskar, C. Mendillo, T. Cook, S. Lockwood,
638 R. Narayanan, T. K. Pant, and S. Chakrabarti (2014), Daytime wave characteristics in the
639 mesosphere lower thermosphere region: Results from the Balloon-borne Investigations of
640 Regional-atmospheric Dynamics experiment, J. Geophys. Res. Space Physics, 119 (3),
641 doi: 10.1002/2013JA019368.
642 Pfister, L., K.R. Chan, T.P. Bui, S. Bowen, M. Legg, B. Gary, K. Kelly, M. Proffitt, and W. Starr
643 (1993), Gravity Waves Generated by a Tropical Cyclone During the STEP Tropical
644 Field Program: A Case Study, J. Geophys. Res., 98, D5.
645 Piani, C., D. Durran, M. J. Alexander, and J. R. Holton (2000), A numerical study of three-
646 dimensional gravity waves triggered by deep tropical convection and their role in the dynamics
647 of the QBO, J. Atmos. Sci., 57, 3689 – 3702, doi:10.1175/1520-0469(2000)057<3689.
648 Plougonven, R., and F. Zhang (2014), Internal gravity waves from atmospheric jets and fronts,
649 Rev. Geophys., 52, 33-76,doi:10.1002/2012RG000419.

650 Preusse. P., S. D. Eckermann and M. Ern (2008), Transparency of the atmosphere to short
651 horizontal wavelength gravity waves , J. Geophys. Res., 113, D24104,
652 doi:10.1029/2007JD009682.
653 Queney, P., (1948), The problem of air flow over mountains: A summary of theoretical results,
654 Bull. AMS., 29, 16-26.
655 Salby, M. L., R.R. Garcia (1987), Transient response to localized episodic heating in the Tropics,
656 Part1: Excitation and short- time Near field behavior, J. Atmos. Sci., 44(2).
657 Schoeberl, M. R (1985), A ray tracing model of gravity wave propagation and breakdown in the
658 middle atmosphere, J. Geophys. Res., 90, 7999-8010, DOI: 10.1029/JD090iD05p07999.
659 Shin Suzuki, Franz-JosefLubkena, Gerd Baumgarten, Natalie Kaifler, Ronald Eixmann, Bifford
660 P. Williams, Takuji Nakamura (2013), Vertical propagation of a mesoscale gravity wave from
661 the lower to the upper atmosphere, J. Atmos. Sol. Terr. Phys., 97, 29–36.
662 Taori, A., A. Jayaraman, V. Kamalakar (2013), Imaging of mesosphere–thermosphere airglow
663 emissions over Gadanki (13.5 ^{0}N, 79.2 ^{0}E)—first results, J. Atmos. and Sol. Terres. Phys. 93,
664 21-28.
665 Taylor, M.J., W.R.J. Pendleton, S. Clark, H. Takahashi, D. Gobbi, R.A. Goldberg (1997), Image
666 measurements of short-period gravity waves at equatorial latitudes. Journal of Geophysical
667 Research., 102 (D22), 26283–26299.
668 Toshitaka Tsuda, Kazunori Ohnishi, Fusako Isoda, Takuji Nakamura, Robert A. Vincent, Iain M.
669 Reid, Sri Woro B. Harijono, Tien Sribimawati, Agus Nuryanto, Harsono Wiryosumarto (1999),
670 Coordinated radar observations of atmospheric diurnal tides in equatorial regions. Earth Planets
671 Space., 51, 579–592

672 Vadas, S.L., M. J. Taylor, P.-D. Pautet, P. A. Stamus, D. C. Fritts, H.-L. Liu, F. T. S˜ao Sabbas,
673 V. T. Rampinelli, P. Batista, and H. Takahashi (2009), Convection: the likely source of the
674 medium-scale gravity waves observed in the OH airglow layer near Brasilia, Brazil, during the
675 SpreadFEx campaign, Ann. Geophys., 27, 231–259.
676 Venkat Ratnam, M., A. Narendra Babu, V. V. M. Jagannadha Rao, S. Vijaya Baskar Rao, and D.
677 Narayana Rao (2008), MST radar and radiosonde observations of inertia-gravity wave
678 climatology over tropical stations: Source mechanisms, J. Geophys. Res., 113, D07109,
679 doi:10.1029/2007JD008986.
680 Vincent, R. A., and M. J. Alexander (2000), Gravity waves in the tropical lower stratosphere: An
681 observational study of seasonal and interannual variability, J. Geophys. Res., 105, 17,971-
682 17,982.
683 Wrasse, C.M., T. Nakamura, T. Tsuda, H. Takahashi, A.F. Medeiros, M.J. Taylor, D. Gobbi, A.
684 Salatun, Suratno, E. Achmad, A.G. Admiranto (2006), Reverse ray tracing of the mesospheric
685 gravity waves observed at 23^{o}S (Brazil) and 7^{o}S (Indonesia) in airglow imagers, J. Atmos.
686 Sol. Terr. Phys., 68, 163–181.
687 Zhou, X.L., J.R. Holton.,G.L. Mullendore (2002), Forcing of secondary waves by breaking of
688 gravity waves in the mesosphere, J. Geophys. Res., 107, NO. D7, 4058,
689 10.1029/2001JD001204.
690 Zhu, X., (1993), Radiative damping revisited: Parameterization of damping rate in the middle
691 atmosphere, J. Atmos. Sci., 50, 3008-3012.
692

693 **Figure captions:**

694 **Figure 1**. Identification of three wave events (left to right) obtained from the airglow emission
695 intensities originating from O(^{1}S) emissions from Gadanki. The wave crests are emphasized by
696 yellow freehand lines. Motion of waves can be obtained by successive images and the
697 direction of propagation is shown by red arrows. Time of occurrence of events is shown in
698 each image in UT (hh:mm).

699 **Figure 2**. Climatological monthly mean contours of (a) temperature, (b) zonal wind and (c)
700 meridional wind obtained over Gadanki region combining a variety of instruments listed in
701 Table 2.

702 **Figure 3**. Profiles of (a) temperature (b) zonal wind and (c) meridional wind obtained using
703 ERA-interim data products for 17 March 2012, 12 UTC over Gadanki region. Profiles obtained
704 from variety of sources over Gadanki (Gadanki model) listed in Table 2 are also superimposed
705 in the respective panels for comparison. Plots (d)-(e) are same as (a)-(c) but obtained for
706 Hyderabad on 8 March 2010. Temperature profile obtained from MSISE-90 and zonal and
707 meridional winds obtained from HWM 07 for the same day are also provided in the respective
708 panels.

709 **Figure 4**. (a) Profile of eddy diffusitvity (thick red line) obtained from Gadanki MST radar (Rao
710 et al., 2001) in the tropopshere, lower stratopshere and mesopshere. Fitted profile (dotted line)
711 with exponetial function is also shown. Hocking's (Hocking 1991) analytical curve
712 (extrapolated) is also superimposed for comparsion. (b) Profiles of eddy, molecualr, and total
713 diffusivity. (c) radiative, and diffusive damping rates.

714 **Figure 5**. Ray paths for the wave event G1 (started at 97 km) in the (a) Longitude-Altitude, (b)
715 Latitude-Altitude, and (c) Longitude-Latitude cross sections. Ray paths obtained while

716 considering different background wind conditions (normal wind, zero wind and Gadanki model
717 wind) and the day-to-day variability of tides are also superimposed (dotted lines). (d)-(f) same
718 as (a)-(c) but for the wave event H1. Note that Gadanki atmospheric model wind is not used for
719 the wave events over Hyderabad.

720 **Figure** 6. Profiles of (a) square of vertical wave number (m^2), (b) intrinsic frequency (ω_{ir}) and
721 Brunt Väisälä frequency (N) (green), (c) horizontal wavelength (d) zonal, (e) meridional, and
722 (f) vertical group velocities for the wave event G1. Profiles of the same obtained while
723 considering the three different background winds (different colored lines) and the day-to-day
724 variability of tides are also superimposed (dotted lines) in the respective panels. The
725 observation time at the ray-start and according times along the ray time is also shown in (a)
726 with axis on the top.

727 **Figure 7**. Normalised amplitudes of gravity waves observed for the wave events (a) G1, and (b)
728 H1, over Gadanki and Hyderabad, respectively. Amplitudes with three different background
729 wind conditions along with different tidal amplitudes are also shown.

730 **Figure 8**. Daily mean latitude-longitude section of (a) OLR observed using NOAA products over
731 Indian region on 17 March 2012. (b)-(d) same as (a) but for IRBT observed at 14 UTC, 15
732 UTC, and 20 UTC, respectively. Open (closed) circles in (a) (b-d) depict the terminal points of
733 the ray paths shown in Figure 4.

734 **Figure 9**. Same as Figure 8 but for wave events observed over Hyderabad on 8 March 2010.
735 Note that IRBT is shown only for 10 UTC.

736 **Figure 10**. Latitude-longitude section of vertical shear in the horizontal wind observed using
737 ERA-Interim data products on (a) 17 March 2012 at 10 km, (b) 8 March 2010 at 8 km. Filled

738 circles depicts the terminal points of the ray paths estimated using three different wind
739 conditions and tidal amplitudes.
740 **Figure 11**. Profiles of Richardson number calculated close to the termination point using
741 radiosonde data for (a) Gadanki and (b) Hyderabad locations.
742
743
744
745 **Table captions:**
746 **Table 1**. GW characteristics (direction of propagation (φ), horizontal wavelength (λ_h), period
747 (T), phase speed (C) and intrinsic frequency (ω_{ir})) for events observed over Gadanki (G) and
748 Hyderabad (H). The terminal point locations (latitude, longitude and altitude) are also shown
749 for each event. Conditions leading to the termination for each wave event are also shown.
750 Events for which ray paths terminated at mesospheric altitude are indicated with an asterisk.
751 **Table 2.** Details of instruments, parameters measured, altitude range in which data is available
752 and the duration of the data considered for developing the Gadanki atmospheric model.

Tables:

Events	φ (degrees)	Λh (km)	T (min)	C (m/s)	Longitude (degrees)	Latitude (degrees)	Altitude (km)	ω_{ir} (rad/s)	Termination condition
Gadanki location									
G1	102	85 (26)	18	78	79.9	10.8	13	0.00058	m^2 <0
G2	98	34 (28.9)	9	63	79.4	12.3	17	0.0116	WKB > 1
G3	132	12 (13.6)	6	33	79.2	13.37	96.9*	0.0006	Intrinsic frequency approaching zero
G4	62	134 (40)	12	186	79.14	13.2	92.9*	0.0093	WKB >1
G5	142	16 (2)	8	33	79.9	12.7	66.9*	0.0156	WKB >1 and m^2<0
Hyderabad location									
H1	11	39 (23.7)	16	41	70.2	15.8	10.5	0.0028	WKB >1
H2	16	57 (31.5)	16	59	75.3	16.4	13.5	0.0046	WKB >1
H3	21	74 (39)	16	77	75.9	16.3	14.5	0.0049	WKB >1
H4	11	39 (19.6)	20	32.5	76.3	17.1	67.6*	0.00083	m^2 > limiting condition and intrinsic frequency approaching zero
H5	16	57 (25)	20	48	72.7	15.7	12.5	0.0029	WKB >1
H6	21	74 (31)	20	61.7	74.7	15,8	13.5	0.0035	WKB >1
H7	11	39 (17.7)	23	28	75.8	16.9	68.5*	0.00087	m^2 > limiting condition and intrinsic frequency approaching zero
H8	16	57 (23)	23	41	68.3	14,8	11.5	0.0022	WKB >1
H9	21	74 (27)	23	54	73.4	15.4	13.5	0.0032	WKB >1

Table 1. GW characteristics (direction of propagation (φ), horizontal wavelength (λ_h) (vertical wavelength (λ_z)), period (T), phase speed (C) and intrinsic frequency (ω_{ir})) for events observed over Gadanki (G) and Hyderabad (H). The terminal point locations (latitude, longitude and altitude) are also shown for each event. Conditions leading to the termination for each wave event are also shown. Events for which ray paths terminated at mesospheric altitude are indicated with an asterisk.

Instrument (parameter(s) obtained)	**Altitude range covered**	**Duration of the data considered**
Indian MST radar (U,V)	4-21 km and 65-85 km	1996-2012
Radiosonde (U, V, T)	1-30 km	2006- 2012
Lidar (T)	30-75 km	1998- 2012
Rocket (U, V, T)	22-80 km	1970-1991, 2002-2007
HALOE, HRDI / UARS (T, U, V)	65-110 km	1991- 2000
SABER/TIMED (T)	30-110 km	2002-2012

Table 2. Details of instruments, parameters measured, altitude range in which data is available and the duration of the data considered for developing the Gadanki atmospheric model.

Figures:

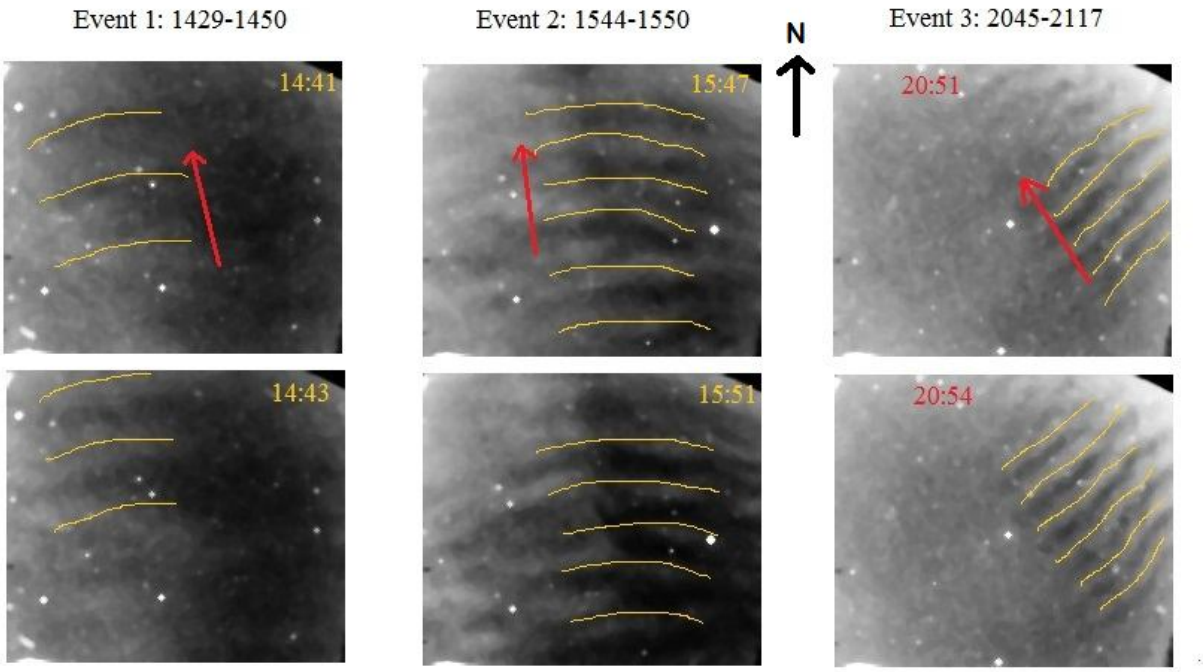

Figure 1. Identification of three wave events (left to right) obtained from the airglow emission intensities originating from O(^{1}S) emissions from Gadanki. The wave crests are emphasized by yellow freehand lines. Motion of waves can be obtained by successive images and the direction of propagation is shown by red arrows. Time of occurrence of events is shown in each image in UT (hh:mm).

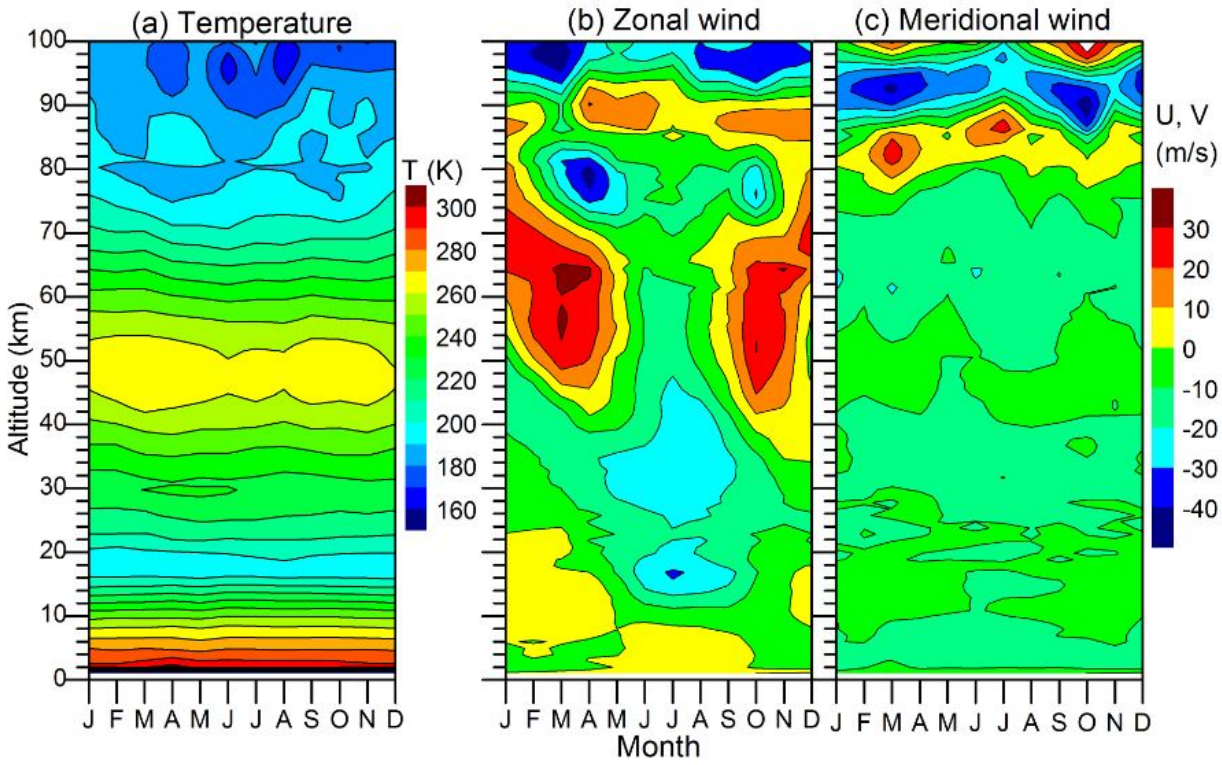

772

773 **Figure 2**. Climatological monthly mean contours of (a) temperature, (b) zonal wind and (c)
774 meridional wind obtained over Gadanki region combining a variety of instruments listed in
775 Table 2.

776

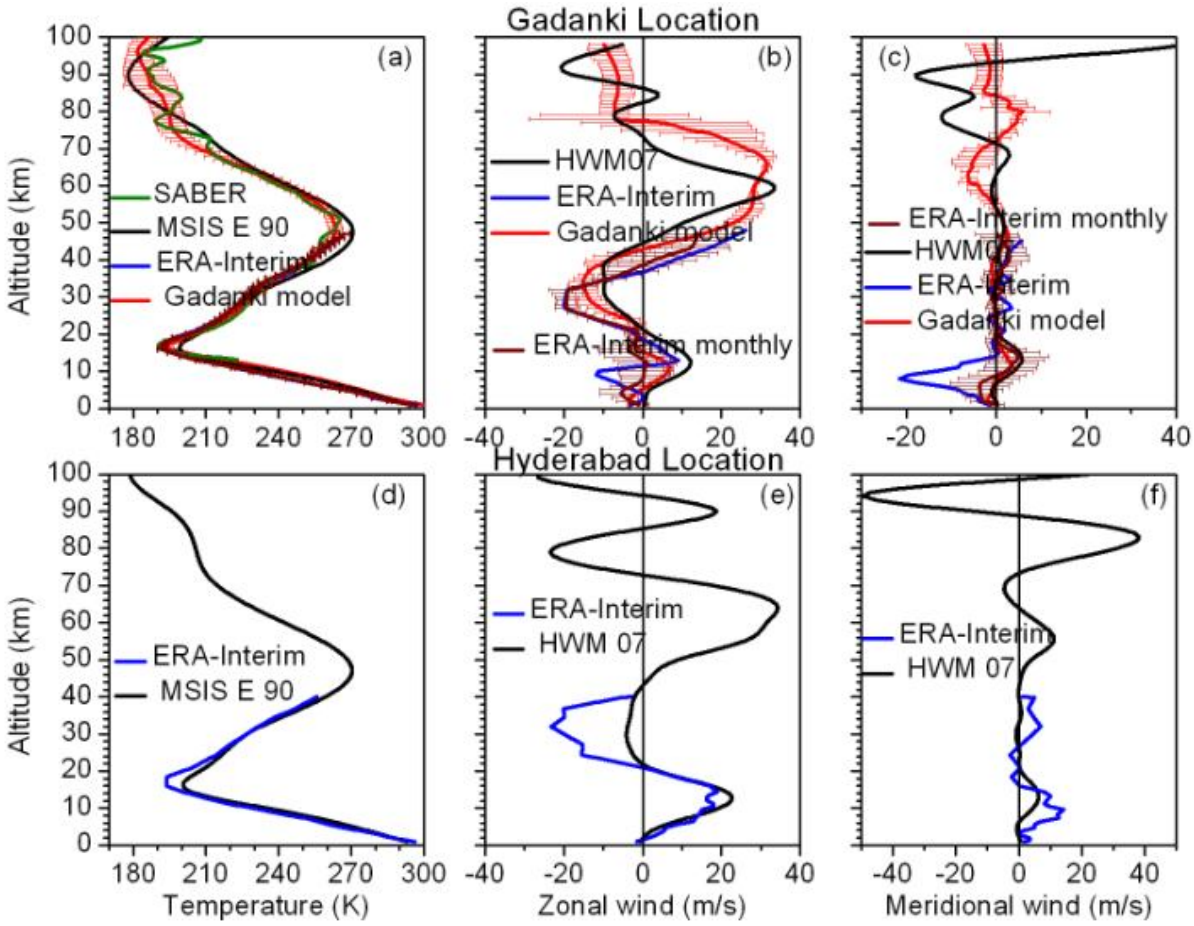

777

778 **Figure 3**. Profiles of (a) temperature (b) zonal wind and (c) meridional wind obtained using
779 ERA-interim data products for 17 March 2012, 12 UTC over Gadanki region. Profiles obtained
780 from variety of sources over Gadanki (Gadanki model) listed in Table 2 are also superimposed
781 in the respective panels for comparison. Plots (d)-(e) are same as (a)-(c) but obtained for
782 Hyderabad on 8 March 2010. Temperature profile obtained from MSISE-90 and zonal and
783 meridional winds obtained from HWM 07 for the same day are also provided in the respective
784 panels.

785

786

787

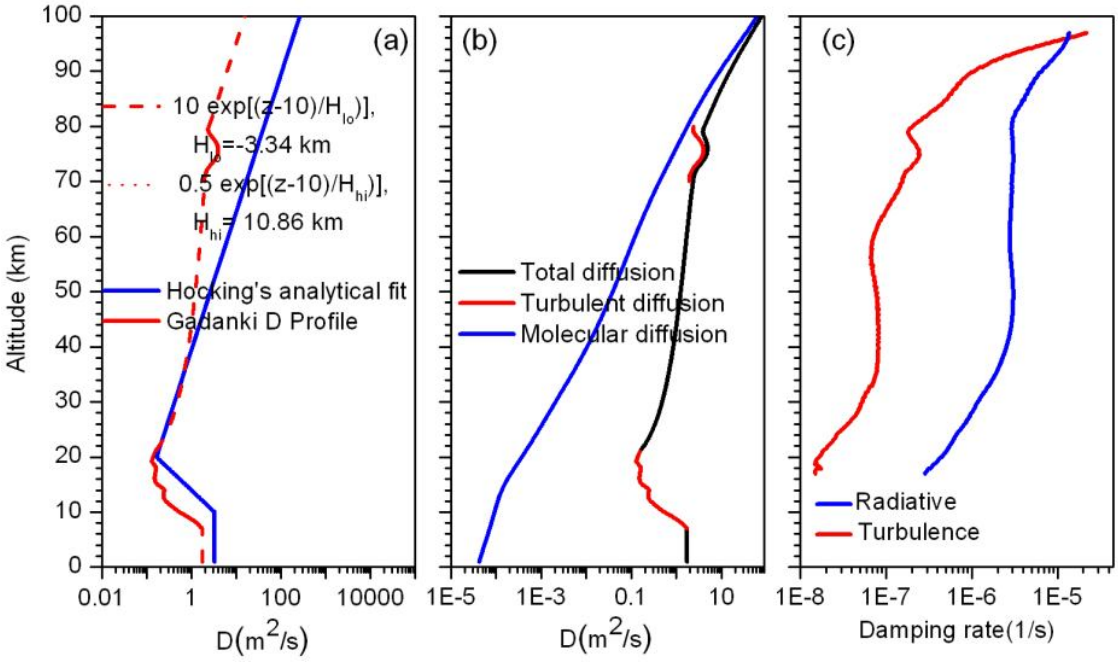

Figure 4. (a) Profile of eddy diffusitvity (thick red line) obtained from Gadanki MST radar (Rao et al., 2001) in the tropopshere, lower stratopshere and mesopshere. Fitted profile (dotted line) with exponetial function is also shown. Hocking's (Hocking 1991) analytical curve (extrapolated) is also superimposed for comparsion. (b) Profiles of eddy, molecualr, and total diffusivity. (c) radiative, and diffusive damping rates.

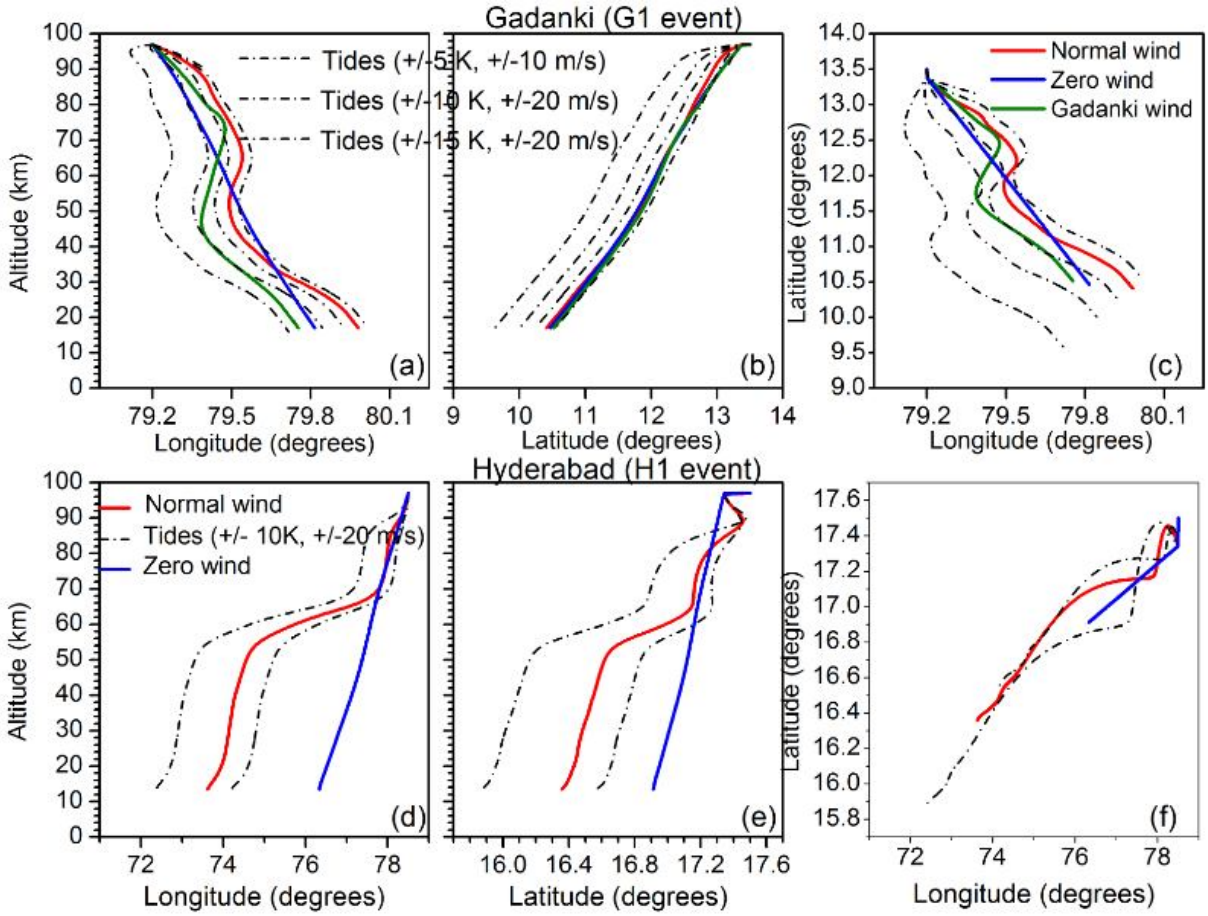

Figure 5. Ray paths for the wave event G1 in the (a) Longitude-Altitude, (b) Latitude-Altitude, and (c) Longitude-Latitude cross sections. Ray paths obtained while considering different background wind conditions (normal wind, zero wind and Gadanki model wind) and the day-to-day variability of tides are also superimposed (dotted lines). (d)-(f) same as (a)-(c) but for the wave event H1. Note that Gadanki atmospheric model wind is not used for the wave events over Hyderabad.

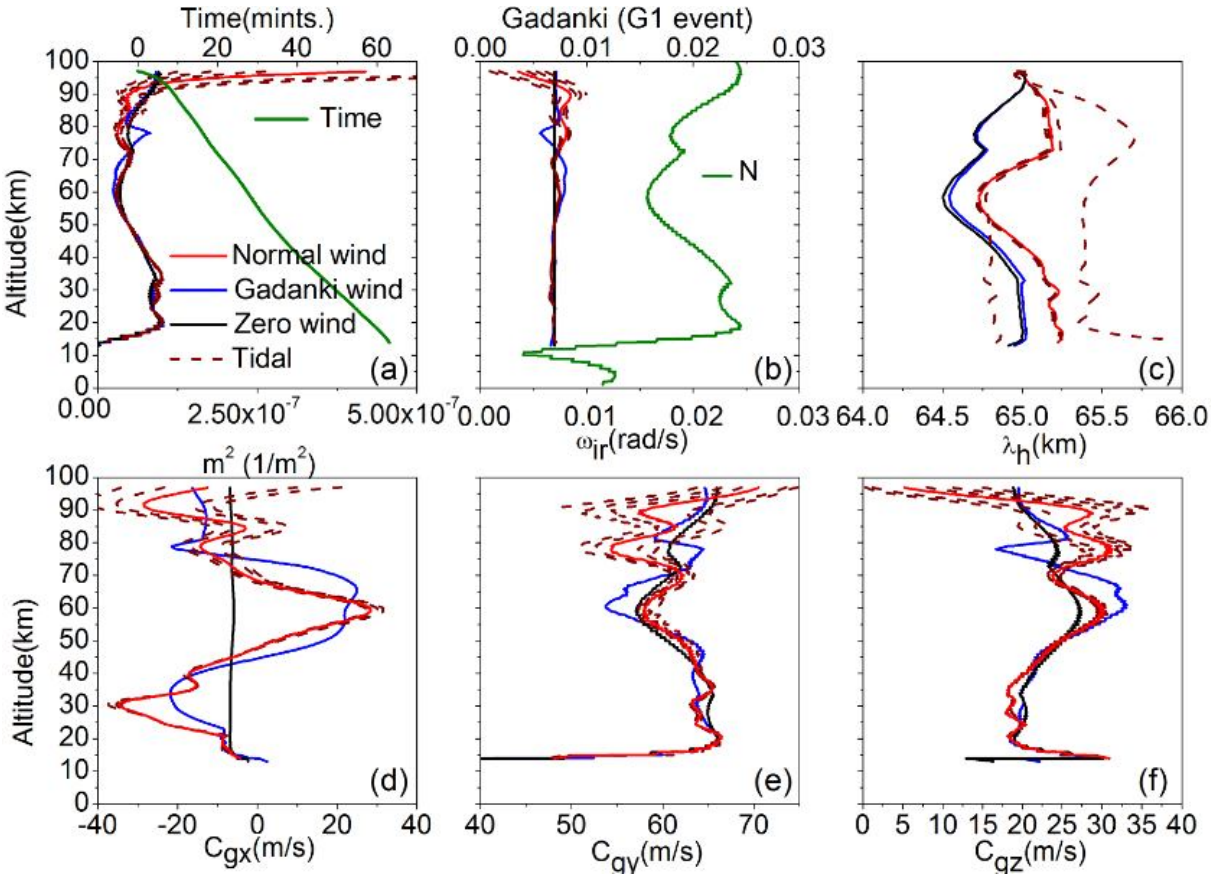

Figure 6. Profiles of (a) square of vertical wave number (m^2), (b) intrinsic frequency (ω_{ir}) and Brunt Väisälä frequency (N) (green), (c) horizontal wavelength (d) zonal, (e) meridional, and (f) vertical group velocities for the wave event G1. Profiles of the same obtained while considering the three different background winds (different colored lines) and the day-to-day variability of tides are also superimposed (dotted lines) in the respective panels. The observation time at the ray-start and according times along the ray time is also shown in (a) with axis on the top.

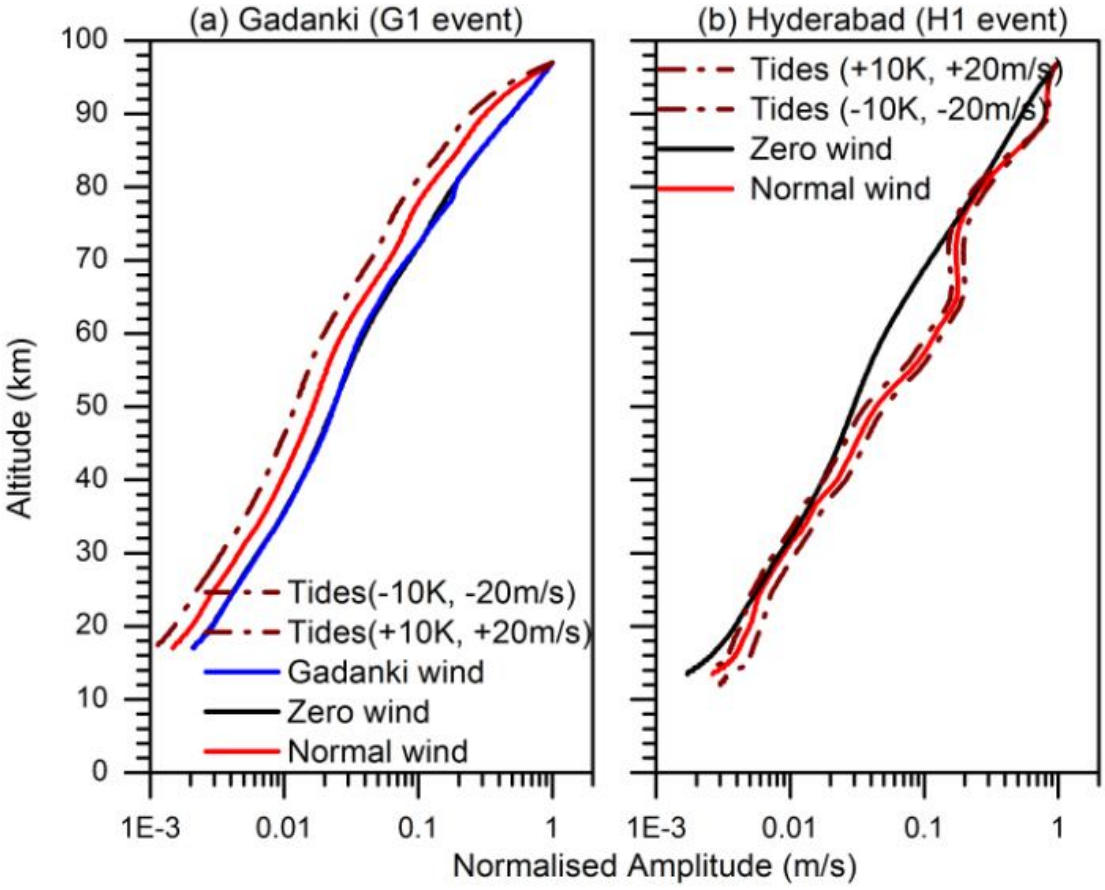

Figure 7. Normalised amplitudes of gravity waves observed for the wave events (a) G1, and (b) H1, over Gadanki and Hyderabad, respectively. Amplitudes with three different background wind conditions along with different tidal amplitudes are also shown.

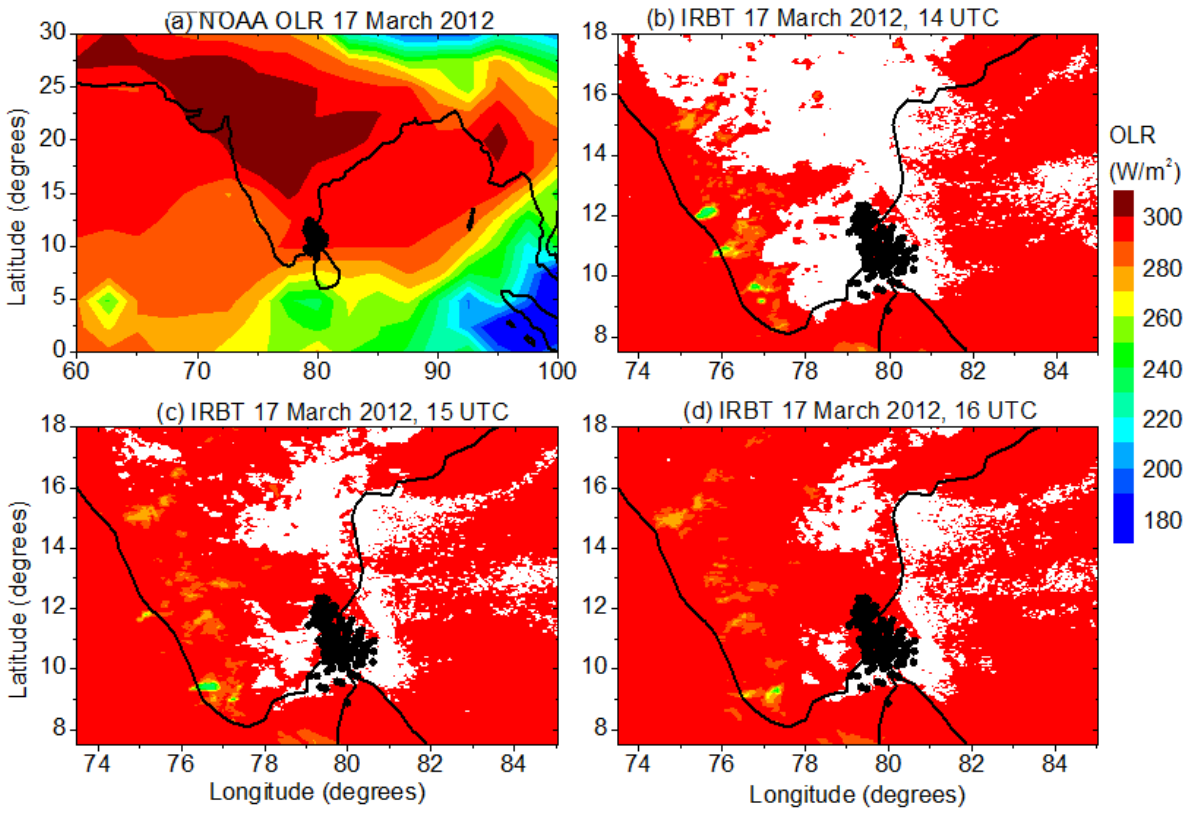

Figure 8. Daily mean latitude-longitude section of (a) OLR observed using NOAA products over Indian region on 17 March 2012. (b)-(d) same as (a) but for IRBT observed at 14 UTC, 15 UTC, and 20 UTC, respectively. Open (closed) circles in (a) (b-d) depict the terminal points of the ray paths shown in Figure 4.

837

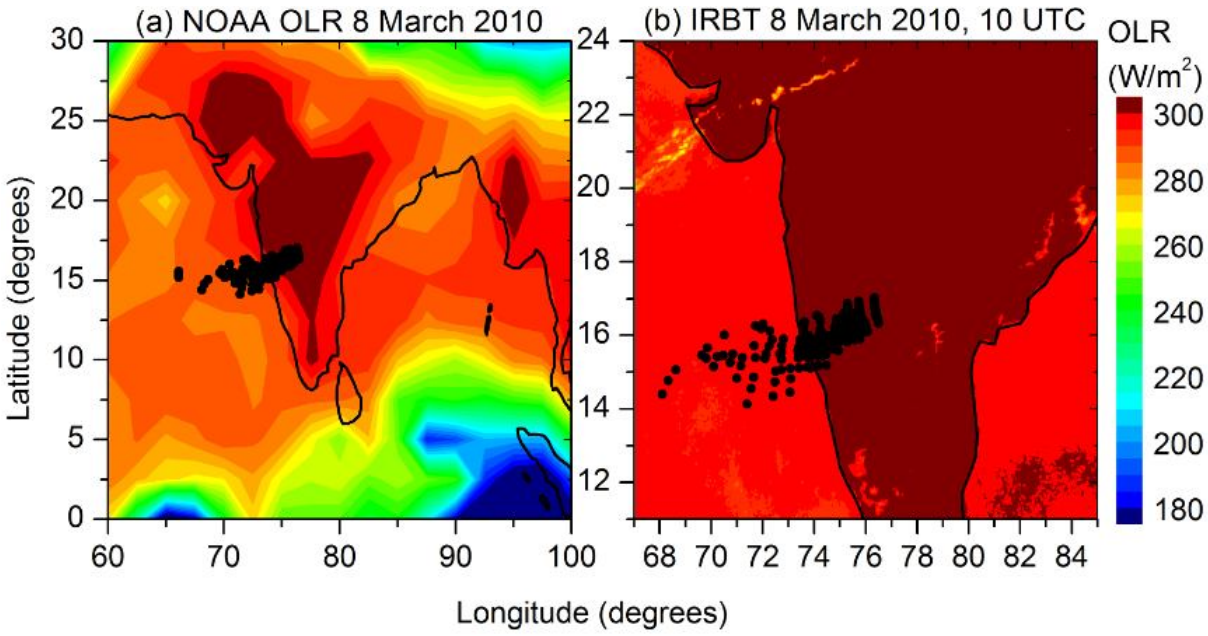

838

839 **Figure 9**. Same as Figure 8 but for wave events observed over Hyderabad on 8 March 2010.

840 Note that IRBT is shown only for 10 UTC.

841

842

843

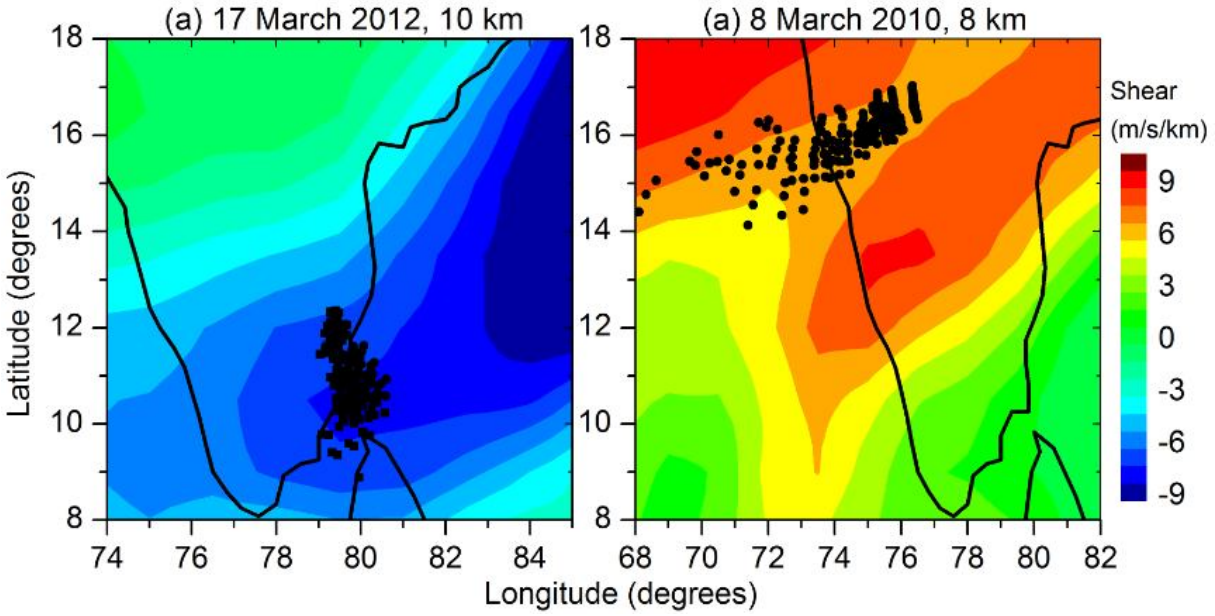

844

845 **Figure 10**. Latitude-longitude section of vertical shear in the horizontal wind observed using
846 ERA-Interim data products on (a) 17 March 2012 at 10 km, (b) 8 March 2010 at 8 km. Filled
847 circles depicts the terminal points of the ray paths estimated using three different wind
848 conditions and tidal amplitudes.

849

850

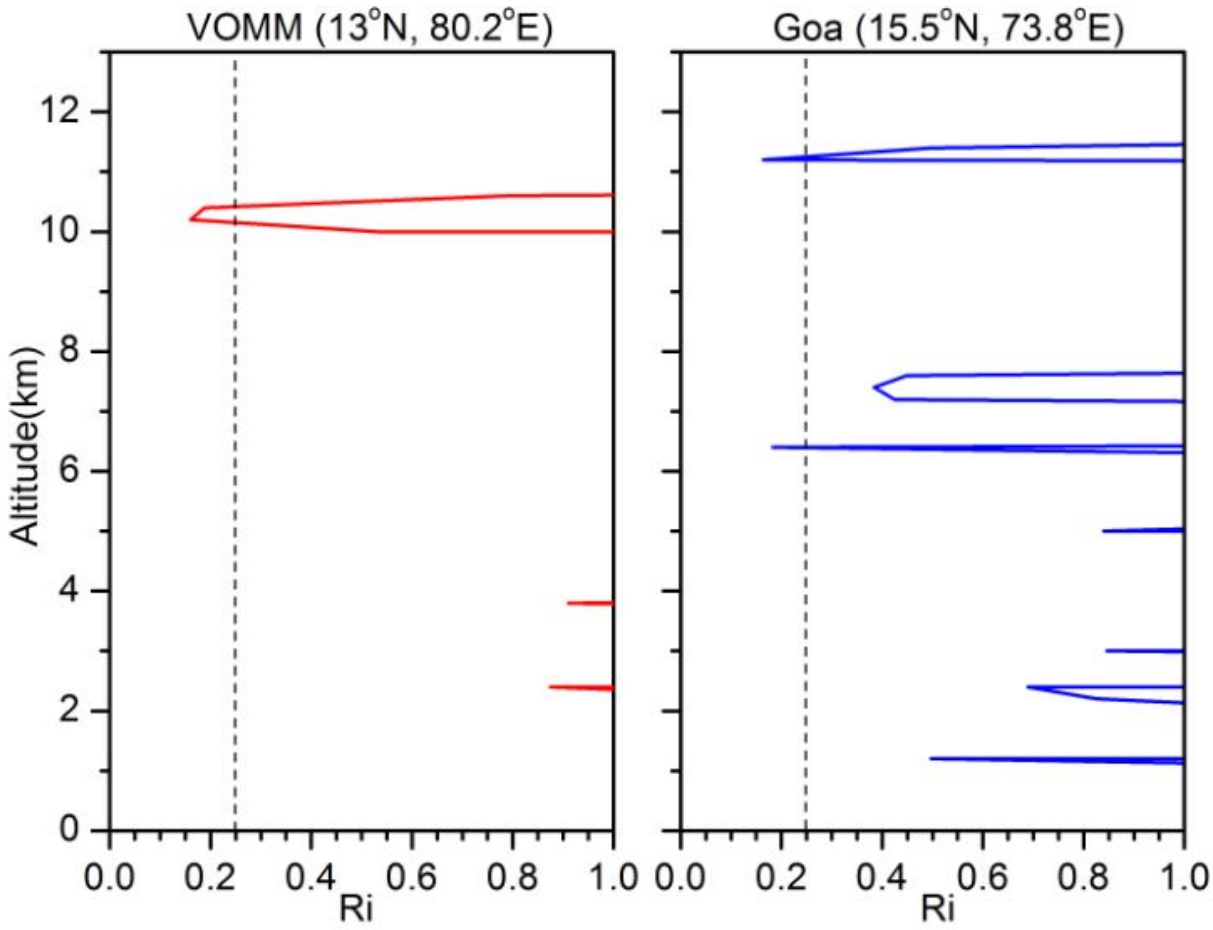

Figure 11. Profiles of Richardson number calculated close to the termination point using radiosonde data for (a) VOMM (Gadanki) and (b) Goa (Hyderabad) locations.